Anisotropic time-resolved solution X-ray scattering patterns from explicit-solvent molecular dynamics

Levin U. L. Brinkmann and Jochen S. Hub

Citation: The Journal of Chemical Physics **143**, 104108 (2015); doi: 10.1063/1.4930013
View online: http://dx.doi.org/10.1063/1.4930013
View Table of Contents: http://scitation.aip.org/content/aip/journal/jcp/143/10?ver=pdfcov
Published by the AIP Publishing

Anisotropic time-resolved solution X-ray scattering patterns from explicit-solvent molecular dynamics

Levin U. L. Brinkmann and Jochen S. Hub[a)]
Institute for Microbiology and Genetics, Georg-August-University Göttingen, Justus-von-Liebig-Weg 11, 37077 Göttingen, Germany

(Received 18 May 2015; accepted 13 August 2015; published online 11 September 2015)

Time-resolved wide-angle X-ray scattering (TR-WAXS) is an emerging experimental technique used to track chemical reactions and conformational transitions of proteins in real time. Thanks to increased time resolution of the method, anisotropic TR-WAXS patterns were recently reported, which contain more structural information than isotropic patterns. So far, however, no method has been available to compute anisotropic WAXS patterns of biomolecules, thus limiting the structural interpretation. Here, we present a method to compute anisotropic TR-WAXS patterns from molecular dynamics simulations. The calculations accurately account for scattering of the hydration layer and for thermal fluctuations. For many photo-excitable proteins, given a low intensity of the excitation laser, the anisotropic pattern is described by two independent components: (i) an isotropic component, corresponding to common isotropic WAXS experiments and (ii) an anisotropic component depending on the orientation of the excitation dipole of the solute. We present a set of relations for the calculation of these two components from experimental scattering patterns. Notably, the isotropic component is not obtained by a uniform azimuthal average on the detector. The calculations are illustrated and validated by computing anisotropic WAXS patterns of a spheroidal protein model and of photoactive yellow protein. Effects due to saturated excitation at high intensities of the excitation laser are discussed, including opportunities to extract additional structural information by modulating the laser intensity. © *2015 AIP Publishing LLC.* [http://dx.doi.org/10.1063/1.4930013]

I. INTRODUCTION

Proteins are flexible nanomachines which frequently carry out their biological function through conformational transitions. An emerging approach to observe proteins in real time is time-resolved wide-angle X-ray scattering (TR-WAXS).[1] This method was successfully applied to observe the structural dynamics of chemical reactions of small molecules in solution.[2–8] More recently, TR-WAXS was applied to track the conformational transitions of photo-active globular proteins[9–16] and proton pumps.[17–20] The structural interpretation of such TR-WAXS signals is challenging since, due to the orientational average inherent to solution X-ray scattering, WAXS patterns contain typically only 10-20 independent data points,[21] whereas proteins contain many more degrees of freedom.

Several studies interpreted TR-WAXS by means of singular value decomposition, thereby detecting the number of conformational intermediates and the kinetics underlying the conformational cycles.[11,12,15] Using such models, scattering curves for structural intermediates and low-resolution real-space electron densities of intermediates could be derived.[15] For a structural interpretation at the atomic level, TR-WAXS patterns have been calculated from structures determined by crystallography[9,10,14,16] or nuclear magnetic resonance (NMR).[13] In addition, Monte Carlo[14] and Molecular Dynamics (MD) simulations[4,5,10,16] have been used to refine structures against WAXS data. For such refinement approaches, due to the low information content of WAXS, a tight *prior* distribution of possible conformational states is required to avoid overfitting of the data.

With the aim to increase the amount of data extracted from TR-WAXS, anisotropic scattering experiments of photoactive yellow protein (PYP) and myoglobin were recently established.[22,23] Anisotropic scattering experiments make use of the fact that a linearly polarized excitation laser primarily excites those proteins whose excitation dipole moment is aligned with the laser polarization. Hence, only photoselectively aligned proteins carry out the photon-induced conformational transition, leading to an anisotropic scattering pattern. In this way, anisotropic WAXS partly overcomes the orientational average, and should therefore provide more independent structural data as compared to isotropic WAXS. The anisotropy of the difference scattering signal decays with the time scale of the rotational diffusion of the protein, which is 10-20 ns for small proteins such as PYP or myoglobin. Methods that allow a structural interpretation of anisotropic WAXS are still limited.[1] Based on anisotropic TR-WAXS data of PYP, Cho and coworkers concluded that PYP shrinks along the axis parallel to the transition dipole and expands in the plane orthogonal to the transition dipole, in qualitative agreement with structures determined by Laue crystallography.[23,24] An atomic-level structural interpretation has so far been complicated by the lack of methods that validate structural models of biomolecules against anisotropic TR-WAXS patterns. A number of studies focussed on predicting

[a)]jhub@gwdg.de; URL: http://cmb.bio.uni-goettingen.de/

anisotropic patterns from X-ray scattering[22,25–29] or electron diffraction,[30] with a focus on small molecules, such as NaI or I_2. These calculations showed that the patterns reduce to two independent components at low excitation intensity. For biomolecules, no method to calculate anisotropic TR-WAXS patterns has been devised.

Isotropic TR-WAXS patterns of biomolecules have so far been calculated from pairs of static structures using implicit solvation models.[9,10,13,14,16] However, such calculations may face limitations in the wide-angle regime, where the internal structure of water and protein fluctuations become relevant.[31–33] In addition, conformational transitions may be subtle, suggesting that side chain and solvent fluctuations must be carefully averaged out before comparing structural models to experimental data. Another disadvantage of simple implicit solvent models is that they require fitting of free parameters associated with the solvation layer and the excluded solvent, thereby reducing the amount of available information. Explicit-solvent MD simulations overcome such limitations. They yield a physically accurate description of solvation, thus avoiding any fitting parameters associated with the solvent, and they naturally account for protein and solvent fluctuations.[33–37]

In this article, we present a method to compute anisotropic TR-WAXS patterns from explicit-solvent MD simulations. The calculations build upon the work by Park *et al.*, who introduced an algorithm to average over explicit solvent configurations taken at frozen solute coordinates.[34] More recently, by using a spatial envelope around the solute and the solvation shell, we extended that algorithm to allow the simultaneous average over solute and solvent degrees of freedom, rendering the protocol directly accessible to unrestrained MD simulation.[33] Noteworthy, those calculations are accessible via the web server WAXSiS.[38] Importantly, our method is not based on the Debye equation that assumes a uniform orientational average, but instead on a numerical orientational average. As shown here, by replacing the uniform with a weighted orientational average, the formalism allows for the calculation of anisotropic patterns.

This article is organized as follows. First, we derive the expression for the calculation of isotropic difference WAXS patterns. This calculation closely resembles the derivation by Park *et al.*, yet the temporal average adopted by Park *et al.* is here replaced by an ensemble average, allowing a more natural generalisation to time-resolved data. Next, the calculation of anisotropic patterns is formulated. We show that, for specific excitation probabilities, the anisotropic patterns can be represented by a sum of two independent components, of which the anisotropic one is subject to an exponential decay due to rotational diffusion. After illustrating the method using a simple test system, we finally validate the calculations by comparing computed isotropic and anisotropic WAXS patterns of PYP to published experimental data. We close with an analysis on the role of saturation effects at high intensities of the excitation laser.

II. THEORY

A. Time-dependent WAXS

We consider a solution of N randomly oriented photoactive proteins, which are excited by a laser pulse at time $t = 0$ (Fig. 1). In a TR-WAXS experiment, the difference in scattering intensity before and after laser excitation is recorded. Hence, we aim to compute the quantity

$$\Delta I(\mathbf{q},\Delta t) = I_{t=\Delta t}(\mathbf{q}) - I_{t<0}(\mathbf{q}), \tag{1}$$

where $I_{t<0}(\mathbf{q})$ is the scattering intensity before laser excitation, and $I_{t=\Delta t}(\mathbf{q})$ is the intensity at a time delay Δt after laser excitation. $\mathbf{q}$ denotes the momentum transfer in the reference frame of the experiment, and it is given through its absolute value q and the azimuthal angle β on the detector, $\mathbf{q} = \mathbf{q}(q,\beta)$. q is related to the scattering angle $2\theta_s$ by $q = 4\pi \sin(\theta_s)/\lambda$, where λ is the wavelength of the X-ray beam.

In the following, $A(\mathbf{r},\Delta t)$ and $B(\mathbf{r})$ denote the electron densities of the solution after and before the laser pulse, respectively. The difference intensity is then given by

$$\Delta I(\mathbf{q},\Delta t) = |\widetilde{A}(\mathbf{q},\Delta t)|^2 - |\widetilde{B}(\mathbf{q})|^2, \tag{2}$$

where $\widetilde{A}$ and $\widetilde{B}$ are the Fourier transforms of A and B, respectively.

In order to evaluate Eq. (2), we decompose the system into disjunct volumes,

$$A(\mathbf{r},\Delta t) = A_b(\mathbf{r}) + \sum_{i\in\mathcal{I}} A_i(\mathbf{r},\Delta t). \tag{3}$$

Here, $\mathcal{I} = \{1,\ldots,N\}$ is a placeholder for the set of N proteins. $A_b(\mathbf{r})$ is the electron density of the bulk solvent, and $A_i(\mathbf{r},\Delta t)$

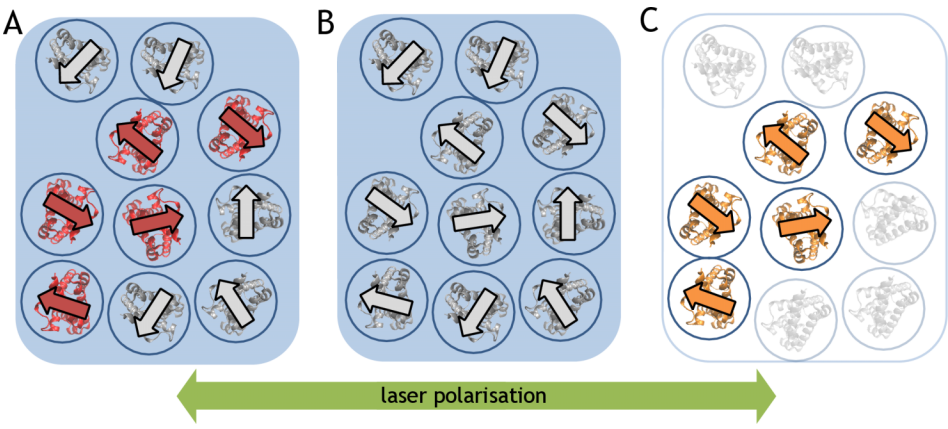

FIG. 1. Illustration of a TR-WAXS experiment. (a) Proteins are randomly oriented in solution. Proteins with the transition dipole moment (arrows) aligned along the laser polarisation (green arrow) are predominantly excited (red). (b) The same ensemble of proteins in solution before excitation. (c) Taking the difference between the solution (b) before and (a) after excitation effectively eliminates contributions from the bulk solvent and from proteins which were not excited (transparent).

is the density of protein i including its solvation layer, to which we refer in the following as *protein droplets*. The volumes contributing to A_i are defined through a constant spatial envelope that encloses the complete conformational space of the protein, up to rotations and translations, as well as its solvation layer (Fig. 3). The construction of the envelope was described in previous work.[33] Analogously, the density before laser excitation is decomposed as $B(\mathbf{r}) = B_b(\mathbf{r}) + \sum_{i\in\mathcal{I}} B_i(\mathbf{r})$. These decompositions are possible if proteins are not aggregated, such that the protein droplets do not overlap.

Expanding the first term in Eq. (2) yields

$$\begin{aligned}|\widetilde{A}(\mathbf{q},\Delta t)|^2 = {}& \widetilde{A}_b(\mathbf{q})\widetilde{A}_b^*(\mathbf{q}) \\ &+ \sum_{i\in\mathcal{I}}\sum_{\substack{j\in\mathcal{I}\\ j\neq i}} \widetilde{A}_i(\mathbf{q},\Delta t)\widetilde{A}_j^*(\mathbf{q},\Delta t) \\ &+ \sum_{i\in\mathcal{I}}\Big[\widetilde{A}_i(\mathbf{q},\Delta t)\widetilde{A}_i^*(\mathbf{q},\Delta t) \\ &+ \widetilde{A}_i(\mathbf{q},\Delta t)\widetilde{A}_b^*(\mathbf{q}) + \widetilde{A}_b(\mathbf{q})\widetilde{A}_i^*(\mathbf{q},\Delta t)\Big]. \quad (4)\end{aligned}$$

Here, the asterisk denotes complex conjugate. An analogous expression can be written for $|\widetilde{B}(\mathbf{q})|^2$.

The first term in Eq. (4) refers to the pure solvent scattering and also depends on the long range organisation of proteins in the A and B systems. Not taking into account solvent heating, these terms should be identical in both systems and hence cancel out. The second term in Eq. (4) yields contributions from protein-protein correlations. For dilute solutions and if q is not close to zero, these contributions can be neglected and, hence, the difference intensity of Eq. (2) is given by

$$\begin{aligned}\Delta I(\mathbf{q},\Delta t) \propto {}& \left\langle|\widetilde{A}_i(\mathbf{q},\Delta t)|^2\right\rangle_{\mathcal{I}} - \left\langle|\widetilde{B}_i(\mathbf{q})|^2\right\rangle_{\mathcal{I}} \\ &+ 2\,\mathrm{Re}\left[\left\langle\widetilde{A}_i(\mathbf{q},\Delta t)\widetilde{A}_b^*(\mathbf{q})\right\rangle_{\mathcal{I}} - \left\langle\widetilde{B}_i(\mathbf{q})\widetilde{B}_b^*(\mathbf{q})\right\rangle_{\mathcal{I}}\right],\end{aligned} \quad (5)$$

where $\mathrm{Re}[\cdot]$ denotes the real part and $\langle\cdot\rangle_{\mathcal{I}}$ indicates the average over all proteins. The first and second term in Eq. (5) correspond to scattering intensities from correlations purely inside the envelopes. The third term, a cross term, originates from correlations between densities inside and outside of the envelope.

In order to evaluate that cross term, we shift each protein into the origin. Accordingly, a shifted electron density for each protein droplet is introduced, $A_i^s(\mathbf{r}-\mathbf{r}_i,\Delta t) = A_i(\mathbf{r},\Delta t)$, where $\mathbf{r}_i$ is the center of mass of protein i, as well as a shifted bulk density $A_{b,i}^s(\mathbf{r}-\mathbf{r}_i) = A_b(\mathbf{r})$. Analogously, all proteins before excitation are shifted into the origin, yielding shifted electron densities of ground-state protein droplets $B_i^s(\mathbf{r})$ and shifted ground-state bulk density $B_{b,i}^s(\mathbf{r})$. The terms in Eq. (5) are invariant under such translations, so we have $\widetilde{A}_i(\mathbf{q},\Delta t)\widetilde{A}_b^*(\mathbf{q}) = \widetilde{A}_i^s(\mathbf{q},\Delta t)\widetilde{A}_{b,i}^{s*}(\mathbf{q})$ and $\widetilde{B}_i(\mathbf{q})\widetilde{B}_b^*(\mathbf{q}) = \widetilde{B}_i^s(\mathbf{q})\widetilde{B}_{b,i}^{s*}(\mathbf{q})$. However, the terms in Eq. (5) do depend on the orientation of the protein. In order to account for different orientations, we decompose the set of proteins into groups $\mathcal{I}(\mathbf{u})$ with identical orientation, denoted by their Euler angle $\mathbf{u}$. Formally, this decomposition can be written as $\mathcal{I} = \bigcap_{\mathbf{u}}\mathcal{I}(\mathbf{u})$, and the average over all proteins is replaced by $\langle\cdot\rangle_{\mathcal{I}} = N_{\mathbf{u}}^{-1}\sum_{\mathbf{u}}\langle\cdot\rangle_{\mathcal{I}(\mathbf{u})}$, where $N_{\mathbf{u}}$ is the number of orientational groups, and $\langle\cdot\rangle_{\mathcal{I}(\mathbf{u})}$ is the average over proteins in group $\mathcal{I}(\mathbf{u})$.

After decomposing the proteins into sets of identical orientation and shifting them to the origin, the cross terms in Eq. (5) can be further simplified. First, we make use of the fact that the distance of the envelope from the protein is large enough, such that correlations between the inside and the outside of the envelope are due to bulk water. Because such correlations can be assumed to be equal before and after laser excitation, we can rewrite[34]

$$\begin{aligned}&\left\langle\widetilde{A}_i^s(\mathbf{q},\Delta t)\widetilde{A}_{b,i}^{s*}(\mathbf{q})\right\rangle_{\mathcal{I}(\mathbf{u})} - \left\langle\widetilde{B}_i^s(\mathbf{q})\widetilde{B}_{b,i}^{s*}(\mathbf{q})\right\rangle_{\mathcal{I}(\mathbf{u})} \\ &\quad\approx \left\langle\widetilde{A}_i^s(\mathbf{q},\Delta t)\right\rangle_{\mathcal{I}(\mathbf{u})}\left\langle\widetilde{A}_{b,i}^{s*}(\mathbf{q})\right\rangle_{\mathcal{I}(\mathbf{u})} \\ &\quad\quad - \left\langle\widetilde{B}_i^s(\mathbf{q})\right\rangle_{\mathcal{I}(\mathbf{u})}\left\langle\widetilde{B}_{b,i}^{s*}(\mathbf{q})\right\rangle_{\mathcal{I}(\mathbf{u})}. \quad (6)\end{aligned}$$

Second, we again make use of the fact that the experiment probes correlations only on the length scale of individual proteins, but not on the protein-protein scale or even on the scale of the entire solution. Consequently, at fixed orientation $\mathbf{u}$, the average shifted bulk density can be approximated by

$$\left\langle B_{b,i}^s(\mathbf{r})\right\rangle_{\mathcal{I}(\mathbf{u})} = \rho_s(1-\Theta_{\mathbf{u}}(\mathbf{r})), \quad (7)$$

where ρ_s is the solvent density and $\Theta_{\mathbf{u}}(\mathbf{r})$ is an indicator function for an envelope of orientation $\mathbf{u}$ and centered at the origin, that is, $\Theta_{\mathbf{u}}(\mathbf{r})$ takes unity inside that envelope and zero outside. By the argument above, we here neglect any "holes" in $B_{b,i}^s(\mathbf{r})$ due to proteins other than protein i, and due to finite size effects of the entire probe volume. The constant in Eq. (7) contributes in reciprocal space only at $\mathbf{q} = \mathbf{0}$, which cannot be measured. Hence, for all relevant $\mathbf{q}$, we have

$$\left\langle\widetilde{B}_{b,i}^s(\mathbf{q})\right\rangle_{\mathcal{I}(\mathbf{u})} = -\rho_s\tilde{\Theta}_{\mathbf{u}}(\mathbf{q}). \quad (8)$$

Third, neglecting solvent heating, we approximate

$$\langle\widetilde{A}_{b,i}^{s*}(\mathbf{q})\rangle_{\mathcal{I}(\mathbf{u})} \approx \langle\widetilde{B}_{b,i}^{s*}(\mathbf{q})\rangle_{\mathcal{I}(\mathbf{u})}. \quad (9)$$

Taking together Eqs. (5), (6), (8), and (9), a difference term can be formulated

$$\begin{aligned}\widetilde{D}_{\mathbf{u}}(\mathbf{q},\Delta t) = {}& \left\langle|\widetilde{A}_i^s(\mathbf{q},\Delta t)|^2\right\rangle_{\mathcal{I}(\mathbf{u})} - \left\langle|\widetilde{B}_i^s(\mathbf{q})|^2\right\rangle_{\mathcal{I}(\mathbf{u})} \\ &- 2\,\mathrm{Re}\left[\left\langle\widetilde{A}_i^s(\mathbf{q},\Delta t) - \widetilde{B}_i^s(\mathbf{q})\right\rangle_{\mathcal{I}(\mathbf{u})}\rho_s\widetilde{\Theta}_{\mathbf{u}}^*(\mathbf{q})\right],\end{aligned} \quad (10)$$

which is calculated from the conformational average of protein droplets in orientation $\mathbf{u}$ before and after excitation. The difference intensity is then obtained as an integral over all possible orientations $\mathbf{u}$,

$$\Delta I(\mathbf{q},\Delta t) \propto \frac{1}{4\pi}\int_{SO(3)} \mathrm{d}\mathbf{u}\,\widetilde{D}_{\mathbf{u}}(\mathbf{q},\Delta t). \quad (11)$$

B. Isotropic case

Let us first consider an isotropic solution, which does not exhibit any correlation between the internal degrees of freedom of the protein and the rotational degrees of freedom. In that case, all $\widetilde{D}_{\mathbf{u}}(\mathbf{q},\Delta t)$ are equal up to a rotation and they can be identified with the difference term in a reference orientation $\widetilde{D}_0(\mathbf{q}'(\mathbf{u}),\Delta t)$ provided that the momentum transfer $\mathbf{q}$ is rotated

likewise. Formally, $\widetilde{D}_{\mathbf{u}}(\mathbf{q},\Delta t)$ can be written as

$$\widetilde{D}_{\mathbf{u}}(\mathbf{q},\Delta t) = \widetilde{D}_0(\hat{R}_{\mathbf{u0}}\mathbf{q},\Delta t) = \widetilde{D}_0(\mathbf{q}'(\mathbf{u}),\Delta t), \tag{12}$$

where $\hat{R}_{\mathbf{u0}}$ denotes the rotation matrix that maps the orientation $\mathbf{u}$ onto the preselected distinguished reference orientation $\mathbf{u}_0$ and consequently defines a rotated momentum $\mathbf{q}'(\mathbf{u}) := \hat{R}_{\mathbf{u0}}\mathbf{q}$. The quantity $\widetilde{D}_0(\mathbf{q}',\Delta t) := \widetilde{D}_{\mathbf{u}=\mathbf{u}_0}(\mathbf{q}',\Delta t)$ denotes the difference term in the reference orientation $\mathbf{u}_0$ and can be computed from a MD simulation, after fitting the protein from all MD snapshots onto a reference structure in orientation $\mathbf{u}_0$. Because of (i) the identity in Eq. (12) and (ii) the invariance of $\tilde{D}_0(\mathbf{q}',\Delta t)$ under rotations around $\mathbf{q}'$, the integration over the three-dimensional Euler angle $\mathbf{u}$ in Eq. (11) can be replaced by an integration over the two dimensional spherical surface $|\mathbf{q}'| = q$,

$$\Delta I_{\mathrm{iso}}(q,\Delta t) \propto \frac{1}{4\pi}\int_{|\mathbf{q}'|=q} \mathrm{d}\mathbf{q}'\tilde{D}_0(\mathbf{q}',\Delta t). \tag{13}$$

For the following discussion, it is important to note that $\mathbf{q}'$ is *not* the momentum transfer $\mathbf{q}$ in the reference frame of the experiment, but instead $\mathbf{q}'$ is the momentum in the reference frame of a protein at fixed protein orientation $\mathbf{u}_0$. Hence, Eq. (13) shows that the integration over all orientations in the frame of the experiment can be replaced by an integration over the surface of a sphere in $\mathbf{q}'$-space (in the reference frame of the protein). Note that this integration depends only on the absolute value q, but not on the azimuthal angle β in the detector. This is consistent with the fact that, in the isotropic case considered here, no anisotropy is expected on the detector.

Equations (13) and (10) are the final result for isotropic time-resolved WAXS, which takes the same mathematical form as the final equation by Park *et al.*[34] for isotropic WAXS. The elaborate discussion on the change of the integration variable was presented here to lay the ground for the calculation of the anisotropic WAXS pattern in the following paragraph.

C. Anisotropic time-dependent WAXS

An anisotropic WAXS pattern is the consequence of an anisotropy in the protein ensemble. In TR-WAXS, the anisotropy in the ensemble follows from the fact that the excitation probability depends on the orientation of the protein. In the following, we consider a two-state system with a ground state G and an excited state E. We assume (i) that all proteins are in the ground state before laser excitation and (ii) that the excitation probability $P(\mathbf{u})$ purely depends on the protein orientation $\mathbf{u}$ but not on any other internal degrees of freedom (Figs. 1(a) and 1(b)). For such a system, it is helpful to decompose the ensemble of proteins after the laser pulse as

$$\left\langle|\widetilde{A}_i^s(\mathbf{q},\Delta t)|^2\right\rangle_{\mathcal{I}(\mathbf{u})} = P(\mathbf{u})\left\langle|\widetilde{E}_i^s(\mathbf{q},\Delta t)|^2\right\rangle_{\mathcal{I}(\mathbf{u})} + [1-P(\mathbf{u})]\left\langle|\widetilde{G}_i^s(\mathbf{q})|^2\right\rangle_{\mathcal{I}(\mathbf{u})} \tag{14}$$

and

$$\left\langle\widetilde{A}_i^s(\mathbf{q},\Delta t)\right\rangle_{\mathcal{I}(\mathbf{u})} = P(\mathbf{u})\left\langle\widetilde{E}_i^s(\mathbf{q},\Delta t)\right\rangle_{\mathcal{I}(\mathbf{u})} + [1-P(\mathbf{u})]\left\langle\widetilde{G}_i^s(\mathbf{q})\right\rangle_{\mathcal{I}(\mathbf{u})}, \tag{15}$$

where $\widetilde{G}$ and $\widetilde{E}$ denote the Fourier transforms of protein droplets in the ground and excited state, respectively. The superscript s indicates again that the densities are shifted to the center-of-mass of the respective solute. $\widetilde{E}$ evolves over time with the conformational transitions after laser excitation, and it therefore depends on the time delay Δt. Before laser excitation, all proteins are in the ground state, so we have

$$\left\langle|\widetilde{B}_i^s(\mathbf{q})|^2\right\rangle_{\mathcal{I}(\mathbf{u})} = \left\langle|\widetilde{G}_i^s(\mathbf{q})|^2\right\rangle_{\mathcal{I}(\mathbf{u})} \tag{16}$$

and

$$\left\langle\widetilde{B}_i^s(\mathbf{q})\right\rangle_{\mathcal{I}(\mathbf{u})} = \left\langle\widetilde{G}_i^s(\mathbf{q})\right\rangle_{\mathcal{I}(\mathbf{u})}. \tag{17}$$

With Eqs. (14)–(17), we obtain the anisotropic version of the difference term (Eq. (10)) as

$$\widetilde{D}_{\mathbf{u}}(\mathbf{q},\Delta t) = P(\mathbf{u})\widetilde{D}'_{\mathbf{u}}(\mathbf{q},\Delta t) \tag{18}$$

with

$$\widetilde{D}'_{\mathbf{u}}(\mathbf{q},\Delta t)\left\langle|\widetilde{E}_i^s(\mathbf{q},\Delta t)|^2\right\rangle_{\mathcal{I}(\mathbf{u})} - \left\langle|\widetilde{G}_i^s(\mathbf{q})|^2\right\rangle_{\mathcal{I}(\mathbf{u})} - 2\,\mathrm{Re}\left[\left\langle\widetilde{E}_i^s(\mathbf{q},\Delta t) - \widetilde{G}_i^s(\mathbf{q})\right\rangle_{\mathcal{I}(\mathbf{u})}\rho_s\widetilde{\Theta}_{\mathbf{u}}^*(\mathbf{q})\right]. \tag{19}$$

Figure 1(c) presents an illustration of Eqs. (18) and (19).

For the isotropic case (Eq. (13)), the integration over orientations $\mathbf{u}$ could be replaced by a uniform integration over the momentum $\mathbf{q}'$ in the reference frame of the protein. For the anisotropic case, additional consideration is required: for a fixed momentum transfer $\mathbf{q}$ in the frame of the experiment, a momentum $\mathbf{q}'$ in the reference frame of the protein defines the orientation of the protein only in two of three dimensions. The missing degree of freedom is a rotation of the protein around $\mathbf{q}$ (or $\mathbf{q}'$, depending on the frame of reference), which we denote by the angle ψ. Hence, for a given momentum $\mathbf{q}$, the orientation $\mathbf{u}(\mathbf{q}',\psi \mid \mathbf{q})$ of the protein is uniquely described by $\mathbf{q}'$ and ψ. The difference intensity is obtained by an integration over the surface of a sphere in q'-space and an integration over the angle ψ,

$$\begin{aligned}\Delta I(\mathbf{q},\Delta t) &\propto \frac{1}{8\pi^2}\int_0^{2\pi}\mathrm{d}\psi\int_{|\mathbf{q}'|=q}\mathrm{d}\mathbf{q}'P(\mathbf{u}(\mathbf{q}',\psi\mid\mathbf{q}))\tilde{D}'_0(\mathbf{q}',\Delta t)\\ &= \frac{1}{4\pi}\int_{|\mathbf{q}'|=q}\mathrm{d}\mathbf{q}'w(\mathbf{q}'\mid\mathbf{q})\tilde{D}'_0(\mathbf{q}',\Delta t),\end{aligned} \tag{20}$$

where $\widetilde{D}'_0(\mathbf{q}',\Delta t)$ is computed in the reference orientation $\mathbf{u}_0$. Again, $\widetilde{D}'_0(\mathbf{q}',\Delta t)$ can be computed from MD simulation snapshots of proteins in the ground and excited state, after fitting the frames onto a reference structure of orientation $\mathbf{u}_0$. In Eq. (20), only the excitation probability $P(\mathbf{u}(\mathbf{q}',\psi|\mathbf{q}))$ depends on ψ, but not the difference term. The integration of $P(\mathbf{u}(\mathbf{q}',\psi|\mathbf{q}))$ over ψ can therefore be conducted separately from the average over protein conformations yielding the weight $w(\mathbf{q}'\mid\mathbf{q}) = \int \mathrm{d}\psi\, P(\mathbf{u}(\mathbf{q}',\psi\mid\mathbf{q}))$.

D. Excitation probability proportional to $\cos^2(\phi)$

In numerous photoactive systems, the excitation probability was found to be proportional to $\cos^2(\phi)$, with ϕ denoting the angle between the excitation dipole moment $\mathbf{m}$

and the polarization vector $\mathbf{l}$ of a linearly polarized laser. We split the excitation probability $P_{\cos^2}(\mathbf{u}) = p_{\text{tot}} p_{\cos^2}(\mathbf{u})$ into the total excitation probability p_{tot} and a normalized orientational probability $p_{\cos^2}(\mathbf{u})$. Taking $\mathbf{l}$ and $\mathbf{m}$ as normalized vectors, we have for the orientational probability

$$p_{\cos^2}(\mathbf{u}) = 3[\mathbf{l} \cdot \mathbf{m}(\mathbf{u})]^2, \tag{21}$$

where $\mathbf{m}(\mathbf{u})$ depends on the orientation $\mathbf{u}$ of the protein.

As shown in Appendix A, evaluating the integral over ψ in Eq. (20) yields

$$\frac{1}{2\pi} \int_0^{2\pi} \mathrm{d}\psi\, p_{\cos^2}(\mathbf{u}(\mathbf{q}', \psi|\mathbf{q})) = [f(\mathbf{q}) w_{\mathbf{m}}(\mathbf{q}') + 1], \tag{22}$$

where we introduced the factor

$$f(\mathbf{q}) = \frac{3}{2}\left(\frac{\mathbf{l} \cdot \mathbf{q}}{q}\right)^2 - \frac{1}{2}, \tag{23}$$

which depends on the angle between $\mathbf{l}$ and $\mathbf{q}$, as well as a weight function

$$\begin{aligned} w_{\mathbf{m}}(\mathbf{q}') &= 3\left(\frac{\mathbf{m} \cdot \mathbf{q}'}{q}\right)^2 - 1 \\ &= 3\cos^2(\theta) - 1 \\ &\propto Y_2^0(\theta), \end{aligned} \tag{24}$$

which is a function of the angle θ between the momentum $\mathbf{q}'$ and the transition moment $\mathbf{m}$. Notably, the weight $w_{\mathbf{m}}(\mathbf{q}')$ is proportional to a spherical harmonic of second degree $Y_2^0(\theta)$ and hence orthogonal to an isotropic weight.

Using the result of the integral (22) in Eq. (20) allows one to rewrite the difference intensity

$$\begin{aligned} \Delta I(q, \beta, \Delta t) \propto p_{\text{tot}}[&f(q, \beta) \Delta I_{\mathbf{m}}(q, \Delta t) \\ &+ \Delta I_{\text{iso}}(q, \Delta t)], \end{aligned} \tag{25}$$

where the momentum $\mathbf{q}$ is expressed by its absolute value q and the azimuthal angle β on the detector. Hence, $\Delta I(q, \beta, \Delta t)$ can be expressed by exactly two independent components, the isotropic component $\Delta I_{\text{iso}}(q, \Delta t)$ (Eq. (13)) and an anisotropic component,

$$\Delta I_{\mathbf{m}}(q, \Delta t) = \frac{1}{4\pi} \int_{|\mathbf{q}'|=q} \mathrm{d}\mathbf{q}' w_{\mathbf{m}}(\mathbf{q}') \widetilde{D}_0'(\mathbf{q}', \Delta t). \tag{26}$$

The contribution of $\Delta I_{\text{iso}}(q, \Delta t)$ to $\Delta I(q, \beta, \Delta t)$ is independent of the azimuthal angle β. In contrast, the anisotropic component $\Delta I_{\mathbf{m}}(q, \Delta t)$ contributes with the factor $f(q, \beta)$, leading to an anisotropic scattering pattern.

To summarize this section, an orientational anisotropy in the ensemble of excited proteins leads to a non-zero anisotropic component $\Delta I_{\mathbf{m}}(q, \Delta t)$. As a consequence, the scattering pattern is anisotropic along the azimuthal angle β, as determined by the factor $f(q, \beta)$. Notably, the conformational transition upon excitation determines the components $\Delta I_{\mathbf{m}}(q, \Delta t)$ and $\Delta I_{\text{iso}}(q, \Delta t)$, but the factor $f(q, \beta)$ is independent of the specific system.

E. Rotational diffusion

The anisotropy of the excitation probability $p(\mathbf{u})$ at time $t = 0$ leads to an anisotropic orientational distribution of both, proteins in the excited state *and* proteins that remained in the ground state. However, due to rotational diffusion, the anisotropy in the orientational distributions decays over time. For the sake of simplicity, we consider only isotropic rotational diffusion.

The rotational diffusion constant is defined as $D = \frac{1}{2}\lim_{\delta t \to 0} \langle (\delta \mathbf{u})^2 \rangle / \delta t$, where $\delta \mathbf{u}$ denotes the angle of rotation within time δt. Analogously to translational diffusion, Fick's law determines the time evolution of the orientational distributions via[39]

$$\frac{\partial p(\mathbf{u}, t)}{\partial t} = D \nabla_{\mathbf{u}}^2 p(\mathbf{u}, t), \tag{27}$$

where $\nabla_{\mathbf{u}}^2$ denotes the Laplace operator. As outlined in Appendix B, Eq. (27) can be solved by expanding $p(\mathbf{u}, t)$ into a series of spherical harmonics Y_l^m. For an initial orientational distribution $p(\mathbf{u}, 0) = p_{\cos^2}(\mathbf{u})$, only Y_0^0 and Y_2^0 contribute to $p(\mathbf{u}, t)$; the first being constant in time and the second decaying with a time constant $\tau_2 = 1/(6D)$. Consequently, the time-dependent orientational distribution is

$$p(\mathbf{u}, \Delta t) \propto \left[e^{-6D\Delta t}\left(p_{\cos^2}(\mathbf{u}) - 1\right) + 1\right]. \tag{28}$$

Using Eq. (28) together with Eq. (22) allows one to include the time dependence due to rotational diffusion into Eq. (25), leading to the central result of the present article,

$$\begin{aligned} \Delta I_{\cos^2}(q, \beta, \Delta t) \propto p_{\text{tot}}\big[&e^{-6D\Delta t} f(q, \beta) \Delta I_{\mathbf{m}}(q, \Delta t) \\ &+ \Delta I_{\text{iso}}(q, \Delta t)\big]. \end{aligned} \tag{29}$$

F. Circular absorber

The excitation probability $p_{\cos^2}$ is typical for a linear absorber. The heme molecule is an important example of a circular absorber. Heme absorbs photons that are polarized along the heme's plane, but it does not absorb photons that are polarized along the heme's normal.[40] The normalised excitation probability of circular absorbers can be written as

$$p_{\text{circ}}(\mathbf{u}) = \frac{3}{2}\left[1 - (\mathbf{l} \cdot \mathbf{m}(\mathbf{u}))^2\right]. \tag{30}$$

Here, the vector $\mathbf{m}$ is the normal to the designated plane of absorption. Since this probability is a linear combination of (i) an isotropic probability and (ii) the excitation probability of a linear absorber, one can easily deduce from Eq. (29) the difference intensity for a circular absorber as

$$\begin{aligned} \Delta I_{\text{circ}}(q, \beta, \Delta t) \propto p_{\text{tot}}\big[&-\frac{1}{2} e^{-6D\Delta t} f(q, \beta) \Delta I_{\mathbf{m}}(q, \Delta t) \\ &+ \Delta I_{\text{iso}}(q, \Delta t)\big]. \end{aligned} \tag{31}$$

Thus, the final result for the circular absorber resembles the one of a linear absorber, yet with a prefactor of $-1/2$ for the anisotropic component.

G. Relations to experimental observables

In a typical experimental setup, the X-ray beam is pointing in horizontal x-direction and the detector is positioned behind the sample in the yz-plane, where the y denotes the second horizontal, and z the vertical axis. The excitation laser is pointing in z direction, and the laser polarization vector in

y direction. Each point on the detector is defined through the momentum transfer q and the azimuthal angle β (defined in respect to the y-direction). For such a setup, we have

$$f(q,\beta) = \frac{3}{2}\left(\frac{\mathbf{e}_y \cdot \mathbf{q}}{q}\right)^2 - \frac{1}{2} = \cos^2(\beta)\left(\frac{3}{2} - \frac{3q^2}{8k^2}\right) - \frac{1}{2} \quad (32)$$

where $k = 2n/\lambda$ denotes the wavenumber of the X-ray beam. Eq. (32), together with Equation (29), yields the two-dimensional (2D) projection of the anisotropic difference intensity that is measured by the detector.

Since the pattern contains only two independent components, it is useful to reduce the experimental 2D intensity pattern to the following quantities: (i) intensities along horizontal ($\beta = 0°$) and vertical ($\beta = 90°$) cuts, denoted as ΔI_h and ΔI_v, respectively; (ii) quarter 90°-averages centered along the horizontal ($\beta = 0° \pm 45°$) and the vertical ($\beta = 90° \pm 45°$) axes, denoted as ΔI_{hqa} and ΔI_{vqa}, respectively; and (iii) the azimuthal average, denoted ΔI_{aa}. To facilitate the transfer to experimental data, Table I reports a number of relations that allow for the calculation of experimental observables from the two calculated components $\Delta I_{\mathbf{m}}(q)$ and $\Delta I_{iso}(q)$, or vice versa. We also report relations for a laser polarization parallel to the X-ray beam as well as for circular and elliptically polarized light. The table reports relations only for a linear absorber. The results for a circular absorber are easily obtained by adding a prefactor of $-1/2$ to the anisotropic component.

III. METHODS

A. Prolate spheroid model

As a simple model for a conformational transition of a protein, we considered volume-preserving elongations of a sphere into a prolate spheroid, by scaling the z-axis by a factor $\alpha = 1.1$ and the other two axes by $1/\sqrt{\alpha}$. The densities of the solute and the solvent were assumed to be homogenous, and no fluctuations were considered. Then, the difference term in Eq. (19) follows

$$\frac{\widetilde{D}_0(\mathbf{q}\cdot R)}{\left(\frac{3}{4}\pi R^3 \Delta\rho\right)^2} = |\widetilde{E}_\alpha(\mathbf{q}\cdot R)|^2 - |\widetilde{S}(\mathbf{q}\cdot R)|^2, \quad (33)$$

where R denotes the radius of the sphere and $\Delta\rho$ the density contrast between solute and solvent. $\widetilde{E}_\alpha$ and $\widetilde{S}$ denote the Fourier transforms of a spheroid and of a sphere of unit density and unit volume. The dimensionless difference intensity $\Delta I(q,\beta)/I_0$, with $I_0 = p_{tot}\left(\frac{3}{4}\pi R^3 \Delta\rho\right)^2$, was computed using Eqs. (33) and (25).

The sphere and the spheroid were modelled by a spatial envelope that was constructed from an icosphere of 5120 triangular faces, as described previously.[33] The Fourier transforms of these volumes were computed numerically by subdividing each pyramid, formed by one face and the origin, into 100 volume bins. These bins were sufficiently small to compute the structure factors even at large q. $|\widetilde{S}(\mathbf{q}')|^2$ and $|\widetilde{E}_\alpha(\mathbf{q}')|^2$ were calculated for 1500 $\mathbf{q}'$-vectors per $|\mathbf{q}'|$, which were distributed according to the spiral method.[41]

TABLE I. Relations between experimental observables (row 2-4) and the two components ΔI_{iso} and $\Delta I_{\mathbf{m}}$ (last row). The difference intensities for linear laser polarization parallel (1) and perpendicular (2-6) to the x-ray beam as well as circular (9) and elliptical (10) laser polarization. For the elliptically polarized laser, the intensity of the perpendicular component was taken to be twice the intensity of the perpendicular component. In addition, differences (7, 8) and superpositions (11, 12) are reported that correspond to the anisotropic $\Delta I_{\mathbf{m}}$ and isotropic ΔI_{iso} component, respectively. Symbols are defined in the main text.

Num.	Symbols	Laser polarisation	Sampling of the 2D pattern	Calculation from $\Delta I_{\mathbf{m}}$ and ΔI_{iso}
1	$\Delta I^{\parallel}$	Parallel	Any cut/azimuthal average	$e^{-6Dt}\left(-\frac{1}{2}+\frac{3q^2}{8k^2}\right)\Delta I_{\mathbf{m}}+\Delta I_{iso}$
2	$\Delta I^{\perp}_{aa}$	Perpendicular	Azimuthal average	$e^{-6Dt}\left(\frac{1}{4}-\frac{3q^2}{16k^2}\right)\Delta I_{\mathbf{m}}+\Delta I_{iso}$
3	$\Delta I^{\perp}_{h}$	Perpendicular	Horizontal cut	$e^{-6Dt}\left(1-\frac{3q^2}{8k^2}\right)\Delta I_{\mathbf{m}}+\Delta I_{iso}$
4	$\Delta I^{\perp}_{v}$	Perpendicular	Vertical cut	$e^{-6Dt}\left(-\frac{1}{2}\right)\Delta I_{\mathbf{m}}+\Delta I_{iso}$
5	$\Delta I^{\perp}_{hqa}$	Perpendicular	Horizontal 90°-average	$e^{-6Dt}\left(\frac{\pi+6}{4\pi}-\frac{(3\pi+6)q^2}{16\pi k^2}\right)\Delta I_{\mathbf{m}}+\Delta I_{iso}$
6	$\Delta I^{\perp}_{vqa}$	Perpendicular	Vertical 90°-average	$e^{-6Dt}\left(\frac{\pi-6}{4\pi}-\frac{(3\pi-6)q^2}{16\pi k^2}\right)\Delta I_{\mathbf{m}}+\Delta I_{iso}$
7	$I_{\Delta hv}=\Delta I^{\perp}_{h}-\Delta I^{\perp}_{v}$	Perpendicular	Difference between horizontal and vertical cuts	$e^{-6Dt}\left(\frac{3}{2}-\frac{3q^2}{8k^2}\right)\Delta I_{\mathbf{m}}$
8	$I_{\Delta hvqa}=\Delta I^{\perp}_{hqa}-\Delta I^{\perp}_{vqa}$	Perpendicular	Difference between horizontal and vertical 90°-averages	$e^{-6Dt}\left(\frac{3}{\pi}-\frac{3q^2}{4\pi k^2}\right)\Delta I_{\mathbf{m}}$
9	$\Delta I^{cir}=\frac{1}{2}\Delta I^{\parallel}+\frac{1}{2}\Delta I^{\perp}_{aa}$	Circular	Azimuthal average	$e^{-6Dt}\left(-\frac{1}{8}+\frac{3q^2}{32k^2}\right)\Delta I_{\mathbf{m}}+\Delta I_{iso}$
10	$\Delta I^{elli}=\frac{1}{3}\Delta I^{\parallel}+\frac{2}{3}\Delta I^{\perp}_{aa}$	Elliptical	Azimuthal average	ΔI_{iso}
11	$\Delta I^{\perp}_{h}+\left(2-\frac{3q^2}{4k^2}\right)\Delta I^{\perp}_{v}$	Perpendicular	Superposition of horizontal and vertical cuts	$\left(3-\frac{3q^2}{4k^2}\right)\Delta I_{iso}$
12	$\left(\frac{\pi-6}{4\pi}-\frac{(3\pi-6)q^2}{16\pi k^2}\right)\Delta I^{\perp}_{hqa}+\left(-\frac{\pi+6}{4\pi}+\frac{(3\pi+6)q^2}{16\pi k^2}\right)\Delta I^{\perp}_{vqa}$	Perpendicular	Superposition of horizontal and vertical 90°-averages	$\left(-\frac{3}{\pi}+\frac{3q^2}{4\pi k^2}\right)\Delta I_{iso}$

B. MD simulations of PYP

MD simulations of 50 ns for PYP were conducted in the ground state pG, and in the excited states pR_0, pR_1, and pR_2 following the nomenclature by Schotte *et al.*[24] Initial coordinates for the excited states were taken from crystallographic structures determined by time-resolved Laue crystallography[24] (protein data bank (PDB) codes 4B9O, 4BBT, and 4BBU). Coordinates of the ground state were taken from Ref. 42 (pdb code 1TS7; altLoc A). This ground state structure was chosen because it exhibits identical side chain orientations as the exited state structure. Position-restraining potentials were applied to backbone atoms (force constant 2000 kJ mol^{-1} nm^{-2}), to heavy atoms of the side chains (force constant 500 kJ mol^{-1} nm^{-2}), and to heavy atoms of the chromophore (10 000 kJ mol^{-1} nm^{-2}). This procedure ensured that our calculations averaged over solvent fluctuations, while the heavy atoms of the protein remained in their crystallographic positions.

The proteins were solvated in 17 000 explicit water molecules; no counter-ions were used for neutralization to achieve rapid convergence of the scattering patterns. The protein was described by the Amber03 force field,[43] and the TIP3P water model was applied.[44] Parameters for the chromophore in the ground and the excited state were kindly provided by G. Gronhof. The simulations were conducted by the GROMACS simulation software.[45] The temperature was controlled at 300 K using a stochastic-dynamics integration scheme ($\tau = 0.3$ ps), and the pressure was kept at 1 bar using the weak coupling scheme[46] ($\tau = 1$ ps). The SETTLE[47] algorithm was applied to constrain the bond lengths and angles of water molecules, and LINCS[48] was used to constrain all other bond lengths, allowing for a time step of 2 fs. Electrostatic interactions were calculated using the particle-mesh Ewald method,[49,50] and dispersive interactions were described by a Lennard-Jones potential with a cutoff at 1 nm. The WAXS patterns were computed using snapshots from every 2 ps, after removing the first 5 ns for equilibration (a total of 22 500 frames for each state).

A common envelope $\Theta_0(\mathbf{r})$ was constructed around the protein at a distance of 0.8 nm from all protein atoms of all frames, after fitting the protein onto a reference structure.[33] We have previously shown that an envelope distance of 0.8 nm is sufficient to account for hydration layer effects in solution scattering.[33] A typical snapshot of PYP including its hydration layer, as defined by the envelope, is shown in Fig. 3(a). The difference term $\widetilde{D}_0(\mathbf{q})$ as well as $\Delta I_{\rm iso}(q)$ and $\Delta I_{\mathbf{m}}(q)$ was computed for 80 q-values, using 2000 $\mathbf{q}'$-vectors per q. A monochromatic X-ray source of 12 keV was assumed. Atomic form factors for protein and water were computed as described previously.[33] All averages were calculated for 10 disjunct time bins of the trajectories. The standard error of the mean is reported as a measure of the statistical uncertainty.

C. Excitation saturation

The excitation probability $p_{\cos^2}$ in Eq. (21) is considered as a good approximation for low laser excitation intensities. However, at high laser intensities, saturation plays a major role. Then, the excitation probability is better described by

$$P_{\rm sat}(\mathbf{u}) = p_{\rm tot}\left[1 - e^{-a(\mathbf{l}\cdot\mathbf{m}(\mathbf{u}))^2}\right] \tag{34}$$

with a total excitation probability $p_{\rm tot} = 1 - \sqrt{\pi}\,\mathrm{erf}(\sqrt{a})/(2\sqrt{a})$.[51] Here, a is a factor referring to the excitation energy density, i.e., the excitation laser intensity. The probability in Eq. (34) contains the $p_{\cos^2}$ case in the limit of small a. For the excitation probability of Eq. (34), we numerically solved the integration over ψ in Eq. (20) providing a weight $w(\mathbf{q}'|q,\beta)$ for each combination of momentum transfer $\mathbf{q}'$ in the reference frame of the protein and for each point on the detector $\mathbf{q}(q,\beta)$. Applying these weights in Eq. (20) while integrating the difference term $\widetilde{D}_0(\mathbf{q}')$ yields the 2D scattering pattern.

IV. RESULTS

A. Spheroid model

We illustrate the implication of the above-derived equations using a simple model of a sphere that is distorted into a prolate spheroid. Two cases are considered that differ in orientations of the excitation dipole $\mathbf{m}$ with respect to the elongation axis, namely, $\mathbf{m}$ is either parallel (denoted as $S_\parallel$, Fig. 2(a)) or perpendicular ($S_\perp$, Fig. 2(b)) to the elongation axis. Hence, the initial and final shapes of $S_\parallel$ and $S_\perp$ are identical, but the orientational distribution of excited states differ between the two cases, leading to different intensity patterns.

The isotropic component $\Delta I_{\rm iso}(q)$ (Eq. (13)) and the anisotropic component $\Delta I_{\mathbf{m}}(q)$ (Eq. (26)) are shown in Figs. 2(c) and 2(d), respectively. As expected, $\Delta I_{\rm iso}(q)$ does not depend on the direction of $\mathbf{m}$. In contrast, $\Delta I_{\mathbf{m}}(q)$ highly depends on $\mathbf{m}$, demonstrating that $\Delta I_{\mathbf{m}}(q)$ contains information which is not encoded in $\Delta I_{\rm iso}(q)$ (compare Fig. 2(d) red and blue).

Figure 2(e) presents the azimuthal average on the detector, $I_{\rm aa}(q)$, and Fig. 2(f) shows the difference between the horizontal and vertical 90°-averages, $I_{\Delta{\rm hvqa}}(q)$, which were computed according to Table I. $I_{\Delta{\rm hvqa}}$ is proportional to $\Delta I_{\mathbf{m}}$, whereas $I_{\rm aa}$ represents a linear combination of $\Delta I_{\rm iso}$ and $\Delta I_{\mathbf{m}}$. Hence, the azimuthal average on the detector does *not* correspond to a spherical average in Fourier space. Thus, small-angle X-ray scattering (SAXS) predictions by tools such as Crysol, FoXS, or WAXSiS,[38,52,53] which compute $\Delta I_{\rm iso}$, should not be compared to $I_{\rm aa}$. Instead, relations listed in Table I demonstrate how to compute $\Delta I_{\rm iso}$ from a scattering pattern, allowing direct comparison to such software tools.

The contribution of $\Delta I_{\mathbf{m}}$ to $I_{\rm aa}$ decays over time due to rotational diffusion (Eq. (29)). Hence, $I_{\rm aa}(q)$ gradually converts into a curve that is proportional to $\Delta I_{\rm iso}(q)$ without the requirement of any additional internal conformational transitions of the protein. This finding has implications on the interpretation of TR-WAXS experiments on the timescale of rotational diffusion, as care has to be taken when analysing the time-dependent components of $I_{\rm aa}$ by, for instance, singular value decomposition. Here, rotational diffusion can manifest itself as one or (for anisotropic diffusion) multiple time-scales, which might be confused with internal conformational transitions of the protein. It is interesting to note that, in this example, the anisotropy of the 2D pattern is approximately proportional

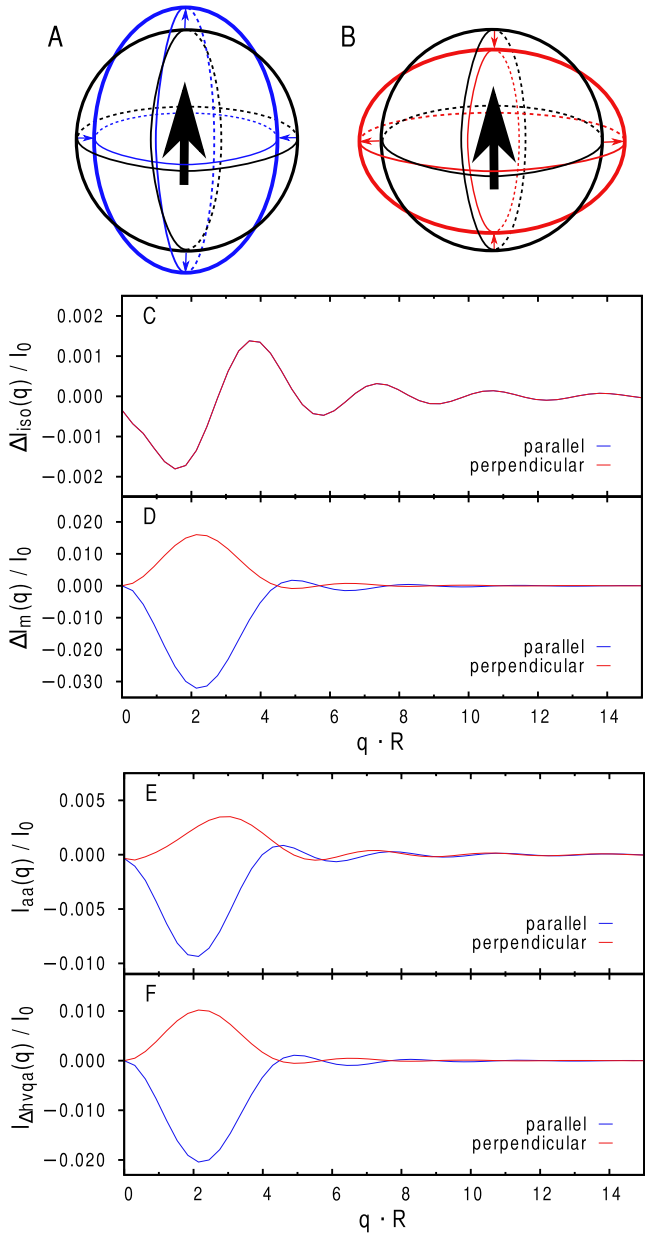

FIG. 2. ((a) and (b)) Model of a globular protein (black). One axis of the sphere is elongated and the other two are contracted to obtain a prolate spheroid of equal volume (colored). The elongated axis is chosen (a) parallel and (b) perpendicular to the transition moment (black arrow). (c) The isotropic component (Eq. (13)), (d) the anisotropic component (Eq. (26)), (e) the azimuthal average, and (f) the difference between horizontal and vertical 90°-averages $I_{\Delta hvqa}$ are plotted in blue and red for the (a) parallel and (b) perpendicular transition moment, respectively. Plotted in a dimensionless fashion neglecting the q/k dependence in Table I. This approximation is valid for $q/k < 0.1$ (e.g., $q < 6$ nm and $k = 60$ nm ≈ 12 keV/($\hbar c$)).

to the elongation factor α. From several calculations with elongation factors in the range $0.9 < \alpha < 1.1$, we found that $\int_0^{4.55} I_{\mathbf{m}}(q)\,dq \approx -0.07\Delta\alpha I_0$, where $\Delta\alpha = \alpha - 1$ quantifies the distortion of the sphere, supporting a similar statement by Cho *et al.*[23]

B. PYP

PYP is a prototypic photoactive protein that undergoes a conformational cycle upon photoexcitation. Hence, conformational transitions of PYP have been studied using various time-resolved methods, including WAXS,[15,23] Laue crystallography,[24,42,54–56] and serial crystallography.[57] Here, we used PYP to validate our methods for the calculation of anisotropic WAXS patterns. Accordingly, WAXS patterns were computed for structures from Laue crystallography and compared to published experimental patterns.[23] Excited state structures pR_0, pR_1, and pR_2 were taken from Anfinrud and coworkers.[24] The backbone atoms of those structures exhibit a very small root mean square deviation (RMSD) of less than 0.21 Å with respect to the ground state. Larger structural differences are mainly found in the vicinity of the chromophore.

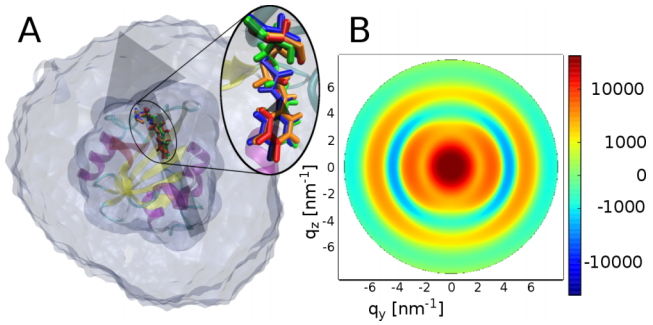

FIG. 3. (a) Cartoon representation of PYP and water molecules within the envelope (grey surface). The chromophore is highlighted as colored sticks in the ground state pG (blue, PDB code 1TS7; altloc A),[42] and in excited states pR_0 (red, 4B9O), pR_1 (orange, 4BBT), and pR_2 (green, 4BBU).[24] The transition dipole along the chromophore is indicated by a black arrow.[23] (b) Two dimensional difference scattering pattern between pR_0 and pG, calculated using Eqs. (25) and (32). The horizontal axis is parallel to the polarization vector of the excitation laser, and the vertical axis is parallel to the excitation laser beam. Intensities in (b) and following plots are presented in e^2/nm normalised by the excitation probability p_{tot} and by the number of proteins N.

1. Anisotropic WAXS of PYP

We computed 2D scattering patterns of the difference intensity between excited states and the ground state using Eqs. (25) and (32) (Fig. 3(b)). Coordinates were taken from molecular dynamics simulations with position restraints on all heavy atoms of the protein (see Sec. III), whereas water coordinates were freely sampled. The azimuthal average I_{aa} and the differences of 90°-averages $I_{\Delta hvqa}$ were derived according to the relations in Table I. Figure 4(a) presents the calculated I_{aa} of pR_0, pR_1, and pR_2 as colored curves. Using the same color coding, Figure 4(b) presents calculated $I_{\Delta hvqa}$. Statistical errors, which were computed by splitting the trajectories into 10 bins, are indicated as shaded areas. The WAXS patterns of pR_0, pR_1, and pR_2 significantly differ, demonstrating that the calculations are able to resolve small conformational transitions on a sub-Ångström scale. In addition, Figure 4 illustrates that the $I_{\Delta hvqa}$ contains information which is not encoded in I_{aa}. For instance, $I_{\Delta hvqa}$ of pR_0 and pR_1 highly differ at 1 nm^{-1}, whereas I_{aa} of pR_0 and pR_1 resemble each other. Hence, the additional information contained in the anisotropy can in principle be utilized to discriminate between different conformational states. To illustrate the effect of rotational diffusion, we computed I_{aa} and $I_{\Delta hvqa}$ for pR_0 at a time delay of 10 ns, assuming a rotational time constant of $1/(6D) = 7.8$ ns

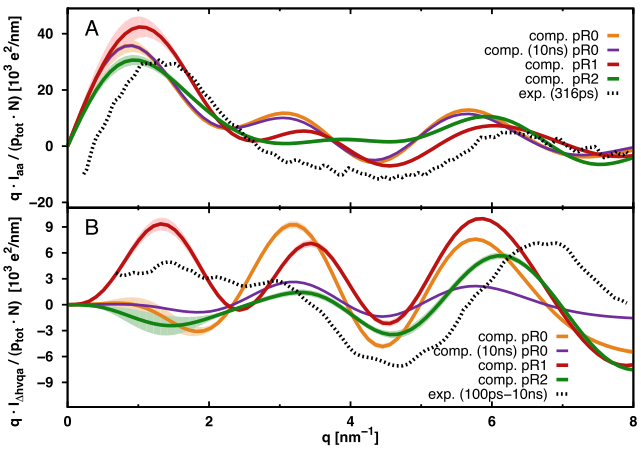

FIG. 4. Difference scattering curves of excited states pR_0 (red), pR_1 (orange), and pR_2 (green) of PYP with respect to the ground state pG. (a) Azimuthal average I_{aa}. (b) The difference between horizontal and vertical azimuthal averaged quarters $I_{\Delta hvqa}$. Violet curves: difference curve for pR_0 including rotational diffusion at a delay time of 10 ns. Black dashed lines: experimental curves for a time delay of 316 ps (a) and delay times average from 100 ps to 10 ns (b), both taken from Ref. 23. The scale of the experimental curves is arbitrary.

(Figs. 4(a) and 4(b), purple curves).[58] For PYP, $I_{\Delta hvqa}$ quickly decays with time whereas I_{aa} is hardly affected by rotational diffusion.

For the sake of completeness, Fig. 4 presents experimental TR-WAXS curves taken from Cho *et al.* as dotted curves.[23] Figure 4(a) shows experimental data at a time delay of 316 ps, at which pR_0 and pR_1 were suggested as the dominant crystallographic conformations.[24] Figure 4(b) presents the $I_{\Delta hvqa}$ curve that had been reported as a logarithmic time average between 100 ps and 10 ns. Overall, some similarity is found between the experimental data and the curves computed from the crystallographic structures, suggesting that the conformational transition in the crystal at least partly resembles the transition in solution on the nanosecond time scale. However, none of the crystallographic structures yield quantitative agreement with the experimental curves. These remaining discrepancies indicate that the static crystal structures only partly reflect the state in solution. In addition, the lack of protein fluctuations in the position-restrained simulations, as well as the relatively low signal-to-noise ratio in the anisotropic experiment may account for some of the deviations. Hence, additional calculations and experiments will be required to resolve which crystallographic structures (if any) best represent the conformational transitions in solution.

2. On the relation between the sample and scattering anisotropy

As discussed above, $I_{\Delta hvqa}$ encodes structural information that is not contained in I_{iso}. The origin of this additional information may not be obvious since the relations between conformational transitions, $D_0'(\mathbf{q}')$, and the observables $I_{\Delta hvqa}$ and I_{aa} are only little intuitive. Thus, to shed some light on these relations, we illustrate the calculation of $I_{\Delta hvqa}$ and I_{aa} in Fig. 5.

Figures 5(a)-5(d) shows $D_0'(\mathbf{q}')$ as calculated from the pR_0 and pG structures. The subplots A-D show $D_0'(\mathbf{q}')$ on spheres in $\mathbf{q}'$-space at momentum transfers of 1.5, 3.0, 4.6, and 6.1 nm^{-1}, respectively. The figures illustrate that, as expected,[59] $D_0'(\mathbf{q}')$ on the surface of the $\mathbf{q}'$-sphere become increasingly rough with increasing q. The weights used to compute I_{aa} from $D_0'(\mathbf{q}')$ are visualized in Fig. 5(e). These weights are not uniform, demonstrating again that I_{aa} is not equivalent to I_{iso}. In addition, Fig. 5(f) visualizes the weights used to compute the anisotropic observable $I_{\Delta hvqa}$ from $D_0'(\mathbf{q}')$, resembling the spherical harmonic Y_2^0. One consequence of the anisotropic weight shown in Fig. 5(f) is that features in $D_0'(\mathbf{q}')$ near the poles (black dots in Fig. 5) are amplified in $I_{\Delta hvqa}$, such as the positive (red) region at 3.0 nm^{-1} (Fig. 5(b)) or the negative (blue) region at 4.6 nm^{-1} (Fig. 5(c)). Hence, those localized features in $D_0'(\mathbf{q}')$ manifest itself in a positive $I_{\Delta hvqa}$

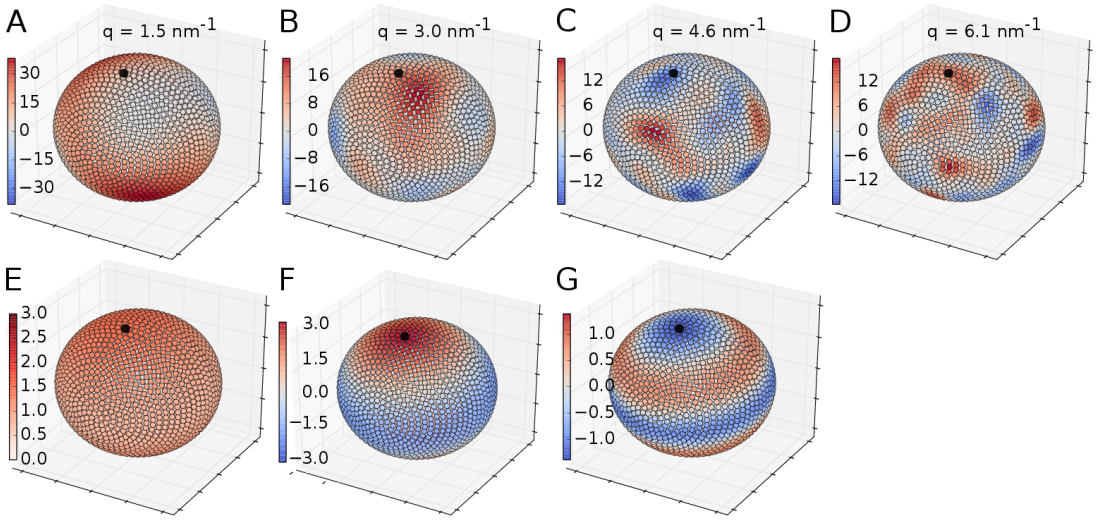

FIG. 5. Difference term $D_0'(\mathbf{q}')$ (Eq. (19)), calculated from the structures pR_0 and pG on a unit sphere, for momenta (a) $q = 1.5$ nm^{-1}, (b) $q = 3.0$ nm^{-1}, (c) $q = 4.6$ nm^{-1}, and (d) $q = 6.1$ nm^{-1}. ((e)-(g)) Weights $w(\mathbf{q}'|q)$ (Eq. (20)) for the calculation of (e) I_{aa}, (f) $I_{\Delta hvqa}$, and (g) $I_{\Delta hvd}$. Each dot corresponds to one $\mathbf{q}'$-vector. The orientation of the sphere corresponds to the orientation of the protein in Fig. 3(a). The direction of the transition moment $\mathbf{m}$ is indicated by a black dot (large arrow in Fig. 3(a)).

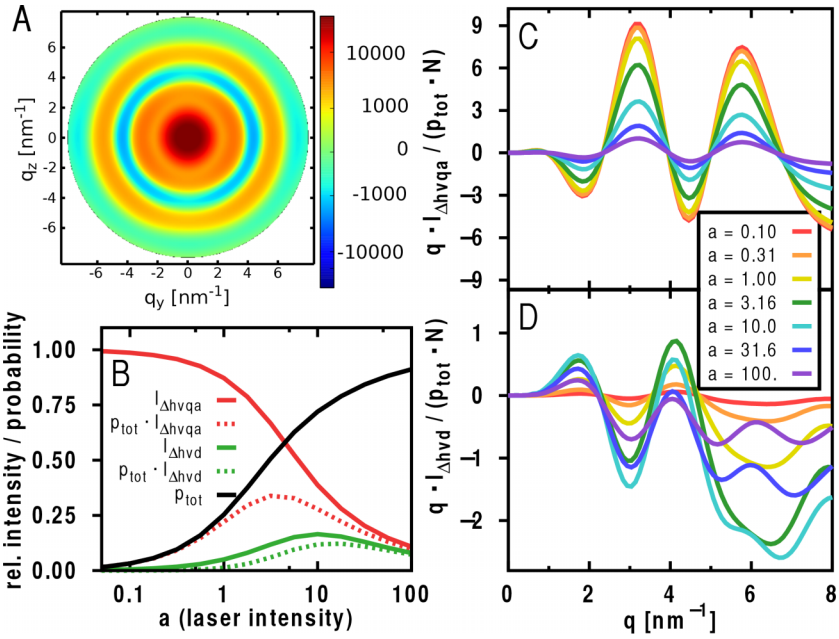

FIG. 6. (a) Scattering pattern of pR_0 and pG for a high excitation laser intensity ($a = 10$). (b) Scattering intensity (red) $I_{\Delta hvqa}(q = 3.0\ \text{nm}^{-1})$ and (green) $I_{\Delta hvd}(q = 3.0\ \text{nm}^{-1})$ (ignoring sign) calculated from 2D scattering pattern for increasing excitation laser intensities. Intensities reported in relation to $I_{\Delta hvqa}(q = 3.0\ \text{nm}^{-1})$ in the low intensity limit. Black curve: total orientational excitation probability p_{tot} for corresponding laser intensities. Dashed curve: the product between intensities and probabilities yields an estimate for the signal on the detector and hence, for the signal-to-noise ratio. (c) $I_{\Delta hvqa}$ and (d) $I_{\Delta hvd}$ from calculations of pR_0 and pG for different laser intensities.

at 3.0 nm^{-1} and a negative $I_{\Delta hvqa}$ at 4.6 nm^{-1}. In contrast, due to the more uniform weights entering I_{aa}, such features may not be apparent in I_{aa}.

3. Saturated excitation: additional anisotropic components

So far, we presented results for excitation probability proportional to $p_{\cos^2}(\mathbf{u}) = \cos^2(\phi)$, which strictly holds only at low excitation laser intensities, such that saturation does not play a role. At high excitation laser intensities, as described in Section III C, the excitation probability is better described by Eq. (34). Hence, at high intensity, the 2D scattering pattern is not merely a sum of the two components I_{iso} and $I_{\mathbf{m}}$, but additional components also contribute, as previously pointed out.[26,30] As an additional component, we here analysed the quantity

$$I_{\Delta hvd}(q) = I_h(q) + I_v(q) - 2I_d(q), \tag{35}$$

where $I_d(q)$ denotes the density along the diagonal cuts of the 2D pattern. The corresponding weights $w(\mathbf{q}'|\beta, q)$ are plotted in Fig. 5(g). They are clearly not a superposition of the two components found for unsaturated excitation, but instead resemble a spherical harmonic of fourth degree.

To investigate the role of saturation in TR-WAXS, we computed 2D scattering patterns from the pR_0 and pG structures including saturation effects for excitation energy densities between $a = 0.1$ and $a = 100$. As expected, scattering patterns for $a = 0.1$ are nearly indistinguishable to patterns which do not account for any saturation effects (see Fig. 3(b)). In contrast, at higher intensities, increasing differences to the $p_{\cos^2}$ case emerge. As an example, visual inspection of the pattern computed with $a = 10$ (Fig. 6(a)) shows that the anisotropy was reduced compared to the pattern at low intensities (compare to Fig. 3(b)). To quantify this effect, Fig. 6(b) (red) shows the intensity $I_{\Delta hvqa}(q = 3\ \text{nm}^{-1})$ of the first maximum at saturated laser intensities, normalized with respect to the curve not taking saturation into account (compare to Fig. 4(b)). Indeed, $I_{\Delta hvqa}$ decays with increasing laser intensity as shown in Fig. 6(b) (red solid line), demonstrating a loss of the anisotropy. In contrast, the additional component $I_{\Delta hvd}(q)$ is not relevant at low saturation, but it increases with increasing saturation (Fig. 6(b), green solid line). This finding is further confirmed in Figures 6(c) and 6(d), which show $I_{\Delta hvqa}(q)$ and $I_{\Delta hvd}(q)$ over the entire q range for various laser intensities, demonstrating again that $I_{\Delta hvqa}(q)$ decays whereas $I_{\Delta hvd}(q)$ rises with increasing a.

Multiplying these intensities with the total excitation probability (Fig. 6(b), black curve) at given laser intensity provides an estimate of the magnitude of $I_{\Delta hvqa}$ and $I_{\Delta hvd}$ in the difference pattern (Fig. 6(b), dotted curves). These curves exhibit maxima at $a \approx 3$ ($p_{tot} \approx 0.5$) and $a \approx 18$ ($p_{tot} \approx 0.75$) for the quantities $I_{\Delta hvqa}(q)$ and $I_{\Delta hvd}(q)$, respectively. These results provide an estimate for the laser intensity that yields the best signal-to-noise ratio for $I_{\Delta hvqa}(q)$ and $I_{\Delta hvd}(q)$. It is important to note that increasing a changes only the magnitude of the $I_{\Delta hvqa}(q)$ curve (Fig. 6(c)), while the shape of $I_{\Delta hvqa}(q)$ is nearly unaffected. This finding suggests that the relations shown in Table I, which were derived for low laser intensities, remain a good approximation even at high excitation laser intensities.

V. DISCUSSION

We have presented a method to compute isotropic or anisotropic time-resolved WAXS patterns from explicit-solvent MD simulations. For the example of PYP presented here, simulations were conducted with restrained heavy atoms (but flexible water), in order to compare crystallographic structures to experimental WAXS data. However, the method is equally suitable to compute TR-WAXS patterns from unrestrained simulation after photoexcitation, allowing rigorous validation of non-equilibrium simulations against experimental TR-WAXS data. Work along these lines will be published elsewhere.

As discussed previously,[34] the calculations rely on two assumptions: (i) the hydration layers of the proteins do not overlap, allowing the decomposition of Eq. (3); (ii) correlations between proteins are negligible. These assumptions are best fulfilled at low protein concentration. At higher concentrations, however, proteins may aggregate or exhibit long-range order due to protein-protein repulsions, which may lead to some discrepancies between experiment and calculations at small angles.

Assuming an excitation probability proportional to $\cos^2(\phi)$, the calculation showed that the 2D intensity difference pattern is given by exactly two components, $\Delta I_{\text{iso}}(q)$ and $\Delta I_{\mathbf{m}}(q)$. Here, $\Delta I_{\text{iso}}(q)$ is computed from the uniform orientational average of the solute, that is, $\Delta I_{\text{iso}}(q)$ is the quantity reported by common SAXS prediction software such as WAXSiS, Crysol, or FoXS.[38,52,53] These two components contain independent information because they are computed by projecting the difference term $\widetilde{D}_0(\mathbf{q}')$ onto two different spherical harmonics. Hence, if noise is neglected, an anisotropic WAXS pattern contains exactly twice the information of an isotropic pattern (ignoring the very small angle regime). To estimate the increased information of anisotropic WAXS more rigorously, the information loss due to noise would need quantification using, for instance, the noisy channel theorem.[60] It is important to note that $\Delta I_{\text{iso}}(q)$ is not equivalent to the intensity $\Delta I_{\text{aa}}(q)$ computed from a uniformly weighted azimuthal average on the detector. Instead, $\Delta I_{\text{iso}}(q)$ can be reconstructed from the anisotropic pattern using, for instance, averages over the horizontal and vertical 90°-segments on the detector (Table I).

If a protein contains multiple chromophores, such as phytochrome, the excitation probability is not proportional to $\cos^2(\phi)$. For such cases, the methods shown here are still applicable. However, the integral of Eq. (20) might have to be evaluated numerically, and the final difference patterns might contain additional independent components.

Rotational diffusion leads to a decay of the contribution of $\Delta I_{\mathbf{m}}(q)$ and, hence, to a decay of the anisotropy in the pattern. Consequently, $\Delta I_{\text{aa}}(q)$ decays exponentially towards $\Delta I_{\text{iso}}(q)$ with a time constant of $1/(6D)$. If the analysis of a TR-WAXS experiment is restricted to $\Delta I_{\text{aa}}(q)$, that decay might be misinterpreted in terms of an internal conformational transition. The risk for such a misinterpretation can be reduced by extracting $\Delta I_{\text{iso}}(q)$ and $\Delta I_{\mathbf{m}}(q)$ from the 2D patterns using the relations in Table I. Alternatively, the azimuthal average of a pattern obtained with an elliptically polarized excitation laser (whose intensity perpendicular to the X-ray beam is twice the one parallel to the X-ray beam) naturally corresponds to the isotropic component $\Delta I_{\text{iso}}(q)$. Note that we restricted the analysis here to isotropic rotational diffusion, which strictly holds only for spherical proteins. In general, rotational diffusion is anisotropic and must be described by a 3×3 diffusion tensor. Anisotropic rotational diffusion has been studied in the context of anisotropic fluorescence and it was found that the diffusion process results in up to 6 distinct timescales.[39] In such cases, orientational distribution of the protein is not merely a superposition of two spherical harmonics and, beside $\Delta I_{\mathbf{m}}(q)$, additional anisotropic components may contribute to the scattering patterns. Thus, differentiating between internal and rotational degrees of freedom may be increasingly challenging. MD simulation can in principle be used to characterize anisotropic diffusion, and may thus guide the interpretation of such complex experiments.

High intensities of the excitation laser lead to excitation probabilities that are not proportional to $\cos^2(\phi)$. We could numerically show that this effect allows one to obtain additional structural information, e.g., from the quantity $I_{\Delta\text{hvd}}(q)$. The underlying principle of using saturation to overcome resolution limits, resembles the principle of stimulated emission depletion (STED) superresolution microscopy.[61] Here, we focussed on the consequence of broadening the orientational distribution as compared to $\cos^2(\phi)$ using saturation effects. However, it may be equally possible to generate a narrower orientational distribution by using a perpendicular de-exciting laser beam as done in a microscopic context.[62] Conventional isotropic solution scattering reduces the three-dimensional density to a one-dimensional signal in Fourier space. By measuring the anisotropy taking saturation effects into account, it is in principle possible to reconstruct structural information along an additional dimension. Only the dimension corresponding to the rotation around the excitation dipole remains inaccessible.

VI. CONCLUSIONS

Next-generation light sources, such as free-electron X-ray lasers, provide time-resolution in the femtosecond regime at very high brilliance. They will allow for measurements of anisotropic TR-WAXS patterns of conformational transitions of biomolecules at excellent signal-to-noise ratio. We have presented a method for accurate predictions of anisotropic WAXS patterns based on explicit-solvent MD. The calculations are highly predictive because they fully account for effects from hydration and thermal fluctuations. The analysis of saturation effects suggests that the anisotropic component $I_{\mathbf{m}}$ is obtained at the best signal-to-noise ratio if ~50% of all proteins were excited. Notably, saturation effects at high intensities of the excitation laser open possibilities to extract additional structural information. We expect that the present article lays the ground for a structural interpretation of anisotropic TR-WAXS experiments of biomolecules.

ACKNOWLEDGMENTS

We are grateful to G. Groenhof for sharing the topologies of PYP, and K. Atkovska for carefully reading the manuscript. Financial supported by the Deutsche Forschungsgemeinschaft is gratefully acknowledged (Grant No. HU 1971/1-1).

APPENDIX A: INTEGRATION OVER ψ

Evaluating the integral over ψ in Eq. (20), we get

$$\int_0^{2\pi} \mathrm{d}\psi\, p_{\cos^2}(\mathbf{u}(\mathbf{q}',\psi|\mathbf{q})) = 3\int_{|\mathbf{q}'|=q} \mathrm{d}\psi (\mathbf{l}\cdot\mathbf{m}(\mathbf{q}',\psi))^2 \quad \text{(A1)}$$

$$= 3\int_0^{2\pi} \mathrm{d}\psi \left(\left(\mathbf{l}_\mathbf{q} + \mathbf{l}_\perp\right) \cdot \left(\mathbf{m}_\mathbf{q}(\mathbf{q}') + \mathbf{m}_\perp(\mathbf{q}', \psi)\right)\right)^2 \tag{A2}$$

$$= 3\int_0^{2\pi} \mathrm{d}\psi' \left(l_q m_q(\mathbf{q}') + l_\perp m_\perp(\mathbf{q}') \cos(\psi')\right)^2 \tag{A3}$$

$$= 2\pi \left[3 l_q^2 m_q^2(\mathbf{q}') + \frac{3}{2} l_\perp^2 m_\perp^2(\mathbf{q}')\right] \tag{A4}$$

$$= 2\pi \left[\left(\frac{3}{2} l_q^2 - \frac{1}{2}\right)\left(3 m_q^2(\mathbf{q}') - 1\right) + 1\right] \tag{A5}$$

$$= 2\pi \left[f(\mathbf{q}) w_\mathbf{m}(\mathbf{q}') + 1\right]. \tag{A6}$$

Here, we decomposed the vector $\mathbf{l}$ as $\mathbf{l} = \mathbf{l}_\mathbf{q} + \mathbf{l}_\perp$, where $\mathbf{l}_\mathbf{q} := (\mathbf{l} \cdot \mathbf{q})\mathbf{q}/q^2$ is the component of $\mathbf{l}$ parallel to $\mathbf{q}$, and $\mathbf{l}_\perp := \mathbf{l} - \mathbf{l}_\mathbf{q}$ is the component perpendicular to $\mathbf{q}$. Analogously, we decomposed $\mathbf{m} = \mathbf{m}_\mathbf{q} + \mathbf{m}_\perp$ into components parallel and perpendicular to $\mathbf{q}$. Eq. (A3) uses the orthogonality of the components parallel and perpendicular to $\mathbf{q}$, that is, $\mathbf{l}_\mathbf{q} \cdot \mathbf{m}_\perp = \mathbf{m}_\mathbf{q} \cdot \mathbf{l}_\perp = 0$. The integration variable was changed to the angle $\psi' = \cos^{-1} \frac{\mathbf{m}_\perp \cdot \mathbf{l}_\perp}{l_\perp m_\perp}$ between the $\mathbf{m}_\perp$ and $\mathbf{l}_\perp$, which is defined for the relevant cases of $\mathbf{l}_\perp \neq 0$ and $\mathbf{m}_\perp \neq 0$. After the integration, no cross terms are left in Eq. (A4), leading to the final result of Eq. (A5). The factor $f(\mathbf{q})$ and the weight function $w_\mathbf{m}(\mathbf{q}')$ are defined in the main text.

APPENDIX B: EXPANSION IN SPHERICAL HARMONICS

Equation (27) can be solved by expanding $p(\mathbf{u},t)$ into a series of spherical harmonics Y_l^m of degree l and order m, because they form an orthogonal set of solutions to the Laplace equation, $\nabla_\mathbf{u}^2 Y_l^m = -l(l+1) Y_l^m$. Here, each eigenvalue $-l(l+1)$ corresponds to a time constant $\tau_l = 1/(D\, l(l+1))$ in the decay of $p(\theta,t)$ towards an isotropic distribution.

Assuming that the excitation probability is proportional to $\cos^2(\phi)$, we take for the orientational distribution at $t = 0$,

$$p(\phi,0) = \cos^2(\phi) = 2\sqrt{\pi} Y_0^0 + \frac{4\sqrt{\pi}}{\sqrt{5}} Y_2^0. \tag{B1}$$

Here, $p(\phi,0)$ was written as a linear combination of two spherical harmonics, $Y_0^0 = \frac{1}{2\sqrt{\pi}}$ and $Y_2^0 = \frac{\sqrt{5}}{4\sqrt{\pi}}\left(3\cos^2\phi - 1\right)$; the first being constant in time and the second decaying with a time constant $\tau_2 = 1/(6D)$. Thus, the solution of Eq. (27) under the given initial conditions is

$$p(\theta,t) = e^{-6Dt}\left[3\cos^2\phi - 1\right] + 1. \tag{B2}$$

Following the calculation of Appendix A, we have

$$\begin{aligned} &\frac{1}{2\pi}\int_0^{2\pi} \mathrm{d}\psi\, p_{\cos^2}(\mathbf{u}(\mathbf{q}', \psi|\mathbf{q}), t) \\ &\quad = e^{-6Dt}\left[f(\mathbf{q}) w_\mathbf{m}(\mathbf{q}') + 1 - 1\right] + 1 \\ &\quad = e^{-6Dt} f(\mathbf{q}) w_\mathbf{m}(\mathbf{q}') + 1, \end{aligned} \tag{B3}$$

which leads to the final result of Section II E (Eq. (29)).

[1] R. Neutze and K. Moffat, "Time-resolved structural studies at synchrotrons and x-ray free electron lasers: Opportunities and challenges," Curr. Opin. Struct. Biol. **22**, 651–659 (2012).

[2] R. Neutze, R. Wouts, S. Techert, J. Davidsson, M. Kocsis, A. Kirrander, F. Schotte, and M. Wulff, "Visualizing photochemical dynamics in solution through picosecond x-ray scattering," Phys. Rev. Lett. **87**, 195508 (2001).

[3] J. Davidsson, J. Poulsen, M. Cammarata, P. Georgiou, R. Wouts, G. Katona, F. Jacobson, A. Plech, M. Wulff, G. Nyman *et al.*, "Structural determination of a transient isomer of CH_2I_2 by picosecond x-ray diffraction," Phys. Rev. Lett. **94**, 245503 (2005).

[4] H. Ihee, M. Lorenc, T. Kim, Q. Kong, M. Cammarata, J. Lee, S. Bratos, and M. Wulff, "Ultrafast x-ray diffraction of transient molecular structures in solution," Science **309**, 1223–1227 (2005).

[5] Q. Kong, J. H. Lee, A. Plech, M. Wulff, H. Ihee, and M. H. Koch, "Ultrafast x-ray solution scattering reveals an unknown reaction intermediate in the photolysis of $[Ru_3(CO)_{12}]$," Angew. Chem., Int. Ed. **47**, 5550–5553 (2008).

[6] H. Ihee, "Visualizing solution-phase reaction dynamics with time-resolved x-ray liquidography," Acc. Chem. Res. **42**, 356–366 (2009).

[7] M. Christensen, K. Haldrup, K. Bechgaard, R. Feidenhansl, Q. Kong, M. Cammarata, M. L. Russo, M. Wulff, N. Harrit, and M. M. Nielsen, "Time-resolved x-ray scattering of an electronically excited state in solution. Structure of the $^3A_{2u}$ state of tetrakis-μ-pyrophosphitodiplatinate (II)," J. Am. Chem. Soc. **131**, 502–508 (2008).

[8] K. Haldrup, M. Christensen, M. Cammarata, Q. Kong, M. Wulff, S. O. Mariager, K. Bechgaard, R. Feidenhans'l, N. Harrit, and M. M. Nielsen, "Structural tracking of a bimolecular reaction in solution by time-resolved x-ray scattering," Angew. Chem., Int. Ed. **121**, 4244–4248 (2009).

[9] M. Cammarata, M. Levantino, F. Schotte, P. A. Anfinrud, F. Ewald, J. Choi, A. Cupane, M. Wulff, and H. Ihee, "Tracking the structural dynamics of proteins in solution using time-resolved wide-angle x-ray scattering," Nat. Methods **5**, 881–886 (2008).

[10] S. Ahn, K. H. Kim, Y. Kim, J. Kim, and H. Ihee, "Protein tertiary structural changes visualized by time-resolved x-ray solution scattering," J. Phys. Chem. B **113**, 13131–13133 (2009).

[11] H. S. Cho, N. Dashdorj, F. Schotte, T. Graber, R. Henning, and P. Anfinrud, "Protein structural dynamics in solution unveiled via 100-ps time-resolved x-ray scattering," Proc. Natl. Acac. Sci. U. S. A. **107**, 7281–7286 (2010).

[12] M. Cammarata, M. Levantino, M. Wulff, and A. Cupane, "Unveiling the timescale of the R–T transition in human hemoglobin," J. Mol. Biol. **400**, 951–962 (2010).

[13] P. L. Ramachandran, J. E. Lovett, P. J. Carl, M. Cammarata, J. H. Lee, Y. O. Jung, H. Ihee, C. R. Timmel, and J. J. van Thor, "The short-lived signaling state of the photoactive yellow protein photoreceptor revealed by combined structural probes," J. Am. Chem. Soc. **133**, 9395–9404 (2011).

[14] K. H. Kim, S. Muniyappan, K. Y. Oang, J. G. Kim, S. Nozawa, T. Sato, S.-Y. Koshihara, R. Henning, I. Kosheleva, H. Ki *et al.*, "Direct observation of cooperative protein structural dynamics of homodimeric hemoglobin from 100 ps to 10 ms with pump–probe x-ray solution scattering," J. Am. Chem. Soc. **134**, 7001–7008 (2012).

[15] T. W. Kim, J. H. Lee, J. Choi, K. H. Kim, L. J. van Wilderen, L. Guerin, Y. Kim, Y. O. Jung, C. Yang, J. Kim *et al.*, "Protein structural dynamics of photoactive yellow protein in solution revealed by pump–probe X-ray solution scattering," J. Am. Chem. Soc. **134**, 3145–3153 (2012).

[16] H. Takala, A. Bjrling, O. Berntsson, H. Lehtivuori, S. Niebling, M. Hoernke, I. Kosheleva, R. Henning, A. Menzel, J. A. Ihalainen, and S. Westenhoff, "Signal amplification and transduction in phytochrome photosensors," Nature **509**, 245–248 (2014).

[17] M. Andersson, J. Vincent, D. van der Spoel, J. Davidsson, and R. Neutze, "A proposed time-resolved x-ray scattering approach to track local and global conformational changes in membrane transport proteins," Structure **16**, 21–28 (2008).

[18] M. Andersson, E. Malmerberg, S. Westenhoff, G. Katona, M. Cammarata, A. B. Wöhri, L. C. Johansson, F. Ewald, M. Eklund, M. Wulff, J. Davidsson, and R. Neutze, "Structural dynamics of light-driven proton pumps," Structure **17**, 1265–1275 (2009).

[19] E. Malmerberg, Z. Omran, J. S. Hub, X. Li, G. Katona, S. Westenhoff, L. Johansson, M. Andersson, M. Cammarata, M. Wulff, D. van der Spoel, J. Davidsson, A. Specht, and R. Neutze, "Time-resolved WAXS reveals accelerated conformational changes in iodoretinal-substituted proteorhodopsin," Biophys. J. **101**, 1345–1353 (2011).

[20] S. Westenhoff, E. Malmerberg, D. Arnlund, L. Johansson, E. Nazarenko, M. Cammarata, J. Davidsson, V. Chaptal, J. Abramson, G. Katona, A. Menzel, and R. Neutze, "Rapid readout detector captures protein time-resolved waxs," Nat. Methods **7**, 775–776 (2010).

[21] K. Haldrup, M. Christensen, and M. M. Nielsen, "Analysis of time-resolved x-ray scattering data from solution-state systems," Acta Crystallogr. A **66**, 261–269 (2010).

[22] J. Kim, K. H. Kim, J. G. Kim, T. W. Kim, Y. Kim, and H. Ihee, "Anisotropic picosecond x-ray solution scattering from photoselectively aligned protein molecules," J. Phys. Chem. Lett. **2**, 350–356 (2011).

[23]H. S. Cho, F. Schotte, N. Dashdorj, J. Kyndt, and P. A. Anfinrud, "Probing anisotropic structure changes in proteins with picosecond time-resolved small-angle x-ray scattering," J. Phys. Chem. B **117**, 15825–15832 (2013).
[24]F. Schotte, H. S. Cho, V. R. Kaila, H. Kamikubo, N. Dashdorj, E. R. Henry, T. J. Graber, R. Henning, M. Wulff, G. Hummer *et al.*, "Watching a signaling protein function in real time via 100-ps time-resolved Laue crystallography," Proc. Natl. Acac. Sci. U. S. A. **109**, 19256–19261 (2012).
[25]P. Ho, D. Starodub, D. Saldin, V. Shneerson, A. Ourmazd, and R. Santra, "Molecular structure determination from x-ray scattering patterns of laser-aligned symmetric-top molecules," J. Chem. Phys. **131**, 131101 (2009).
[26]U. Lorenz, K. B. Møller, and N. E. Henriksen, "On the interpretation of time-resolved anisotropic diffraction patterns," New J. Phys. **12**, 113022 (2010).
[27]K. B. Møller and N. E. Henriksen, "Time-resolved x-ray diffraction: The dynamics of the chemical bond," Struct. Bonding **142**, 185–212 (2012).
[28]A. Debnarova, S. Techert, and S. Schmatz, "Computational studies of the x-ray scattering properties of laser aligned stilbene," J. Chem. Phys. **134**, 054302 (2011).
[29]T. Penfold, I. Tavernelli, R. Abela, M. Chergui, and U. Rothlisberger, "Ultrafast anisotropic x-ray scattering in the condensed phase," New J. Phys. **14**, 113002 (2012).
[30]J. S. Baskin and A. H. Zewail, "Oriented ensembles in ultrafast electron diffraction," ChemPhysChem **7**, 1562–1574 (2006).
[31]J. Bardhan, S. Park, and L. Makowski, "*SoftWAXS*: A computational tool for modeling wide-angle x-ray solution scattering from biomolecules," J. Appl. Crystallogr. **42**, 932–943 (2009).
[32]P. B. Moore, "The effects of thermal disorder on the solution-scattering profiles of macromolecules," Biophys. J. **106**, 1489–1496 (2014).
[33]P. Chen and J. S. Hub, "Validating solution ensembles from molecular dynamics simulation by wide-angle x-ray scattering data," Biophys. J. **107**, 435–447 (2014).
[34]S. Park, J. P. Bardhan, B. Roux, and L. Makowski, "Simulated x-ray scattering of protein solutions using explicit-solvent models," J. Chem. Phys. **130**, 134114 (2009).
[35]T. Oroguchi and M. Ikeguchi, "Effects of ionic strength on saxs data for proteins revealed by molecular dynamics simulations," J. Chem. Phys. **134**, 025102 (2011).
[36]J. Köfinger and G. Hummer, "Atomic-resolution structural information from scattering experiments on macromolecules in solution," Phys. Rev. E **87**, 052712 (2013).
[37]P. Chen and J. S. Hub, "Interpretation of solution x-ray scattering by explicit-solvent molecular dynamics," Biophys. J. **108**, 2573–2584 (2015).
[38]C. J. Knight and J. S. Hub, "WAXSiS: A web server for the calculation of SAXS/WAXS curves based on explicit-solvent molecular dynamics," Nucleic Acids Res. **43**, W225–W230 (2015).
[39]W. Huntress, "The study of anisotropic rotation of molecules in liquids by nmr quadrupolar relaxation," Adv. Magn. Opt. Reson. **4**, 1 (1970).
[40]M. Lim, T. A. Jackson, and P. A. Anfinrud, "Binding of Co to myoglobin from a heme pocket docking site to form nearly linear Fe-Co," Science **269**, 962–966 (1995).
[41]Ponti, "Simulation of magnetic resonance static powder lineshapes: A quantitative assessment of spherical codes," J. Magn. Reson. **138**, 288–297 (1999).
[42]H. Ihee, S. Rajagopal, V. Šrajer, R. Pahl, S. Anderson, M. Schmidt, F. Schotte, P. A. Anfinrud, M. Wulff, and K. Moffat, "Visualizing reaction pathways in photoactive yellow protein from nanoseconds to seconds," Proc. Natl. Acad. Sci. U. S. A. **102**, 7145–7150 (2005).
[43]Y. Duan, C. Wu, S. Chowdhury, M. C. Lee, G. Xiong, W. Zhang, R. Yang, P. Cieplak, R. Luo, T. Lee, J. Caldwell, J. Wang, and P. Kollman, "A point-charge force field for molecular mechanics simulations of proteins based on condensed-phase quantum mechanical calculations," J. Comput. Chem. **24**, 1999–2012 (2003).
[44]W. L. Jorgensen, J. Chandrasekhar, J. D. Madura, R. W. Impey, and M. L. Klein, "Comparison of simple potential functions for simulating liquid water," J. Chem. Phys. **79**, 926–935 (1983).
[45]S. Pronk, S. Páll, R. Schulz, P. Larsson, P. Bjelkmar, R. Apostolov, M. R. Shirts, J. C. Smith, P. M. Kasson, D. van der Spoel, B. Hess, and E. Lindahl, "GROMACS 4.5: A high-throughput and highly parallel open source molecular simulation toolkit," Bioinformatics **29**, 845–854 (2013).
[46]H. J. C. Berendsen, J. P. M. Postma, A. DiNola, and J. R. Haak, "Molecular dynamics with coupling to an external bath," J. Chem. Phys. **81**, 3684–3690 (1984).
[47]S. Miyamoto and P. A. Kollman, "SETTLE: An analytical version of the SHAKE and RATTLE algorithms for rigid water models," J. Comput. Chem. **13**, 952–962 (1992).
[48]B. Hess, "P-LINCS: A parallel linear constraint solver for molecular simulation," J. Chem. Theory Comput. **4**, 116–122 (2008).
[49]T. Darden, D. York, and L. Pedersen, "Particle mesh Ewald: An N·log(N) method for Ewald sums in large systems," J. Chem. Phys. **98**, 10089–10092 (1993).
[50]U. Essmann, L. Perera, M. L. Berkowitz, T. Darden, H. Lee, and L. G. Pedersen, "A smooth particle mesh Ewald potential," J. Chem. Phys. **103**, 8577–8592 (1995).
[51]H. Peng and B. G. Barisas, "Saturation effects on phosphorescence anisotropy measurements at high laser pulse energies," J. Fluoresc. **7**, 139–145 (1997).
[52]D. Svergun, C. Barberato, and M. H. J. Koch, "*CRYSOL* – a program to evaluate x-ray solution scattering of biological macromolecules from atomic coordinates," J. Appl. Crystallogr. **28**, 768–773 (1995).
[53]D. Schneidman-Duhovny, M. Hammel, and A. Sali, "FoXS: A web server for rapid computation and fitting of SAXS profiles," Nucleic Acids Res. **38**, W540–W544 (2010).
[54]M. Schmidt, R. Pahl, V. Srajer, S. Anderson, Z. Ren, H. Ihee, S. Rajagopal, and K. Moffat, "Protein kinetics: Structures of intermediates and reaction mechanism from time-resolved x-ray data," Proc. Natl. Acad. Sci. U. S. A. **101**, 4799–4804 (2004).
[55]R. Kort, K. J. Hellingwerf, and R. B. Ravelli, "Initial events in the photocycle of photoactive yellow protein," J. Biol. Chem. **279**, 26417–26424 (2004).
[56]Y. O. Jung, J. H. Lee, J. Kim, M. Schmidt, K. Moffat, V. Šrajer, and H. Ihee, "Volume-conserving trans–cis isomerization pathways in photoactive yellow protein visualized by picosecond x-ray crystallography," Nat. Chem. **5**, 212–220 (2013).
[57]J. Tenboer, S. Basu, N. Zatsepin, K. Pande, D. Milathianaki, M. Frank, M. Hunter, S. Boutet, G. J. Williams, J. E. Koglin *et al.*, "Time-resolved serial crystallography captures high-resolution intermediates of photoactive yellow protein," Science **346**, 1242–1246 (2014).
[58]H. Otto, D. Hoersch, T. E. Meyer, M. A. Cusanovich, and M. P. Heyn, "Time-resolved single tryptophan fluorescence in photoactive yellow protein monitors changes in the chromophore structure during the photocycle via energy transfer," Biochemistry **44**, 16804–16816 (2005).
[59]N. A. Gumerov, K. Berlin, D. Fushman, and R. Duraiswami, "A hierarchical algorithm for fast debye summation with applications to small angle scattering," J. Comput. Chem. **33**, 1981–1996 (2012).
[60]R. P. Rambo and J. A. Tainer, "Super-resolution in solution x-ray scattering and its applications to structural systems biology," Annu. Rev. Biophys. **42**, 415–441 (2013).
[61]S. W. Hell and J. Wichmann, "Breaking the diffraction resolution limit by stimulated emission: Stimulated-emission-depletion fluorescence microscopy," Opt. Lett. **19**, 780–782 (1994).
[62]N. Hafi, M. Grunwald, L. S. van den Heuvel, T. Aspelmeier, J.-H. Chen, M. Zagrebelsky, O. M. Schütte, C. Steinem, M. Korte, A. Munk *et al.*, "Fluorescence nanoscopy by polarization modulation and polarization angle narrowing," Nat. Methods **11**, 579–584 (2014).